ⓞ Geothermal Energy

Interpretation of gravity–magnetic anomalies to delineate subsurface configuration beneath east geothermal province along the Mahanadi rift basin: a case study of non-volcanic hot springs

Aurobindo Kumar Basantaray and Animesh Mandal[*]

*Correspondence:
animeshm@iitk.ac.in
Department of Earth
Sciences, Indian Institute
of Technology Kanpur,
Kanpur 208016, India

Abstract

Gravity and magnetic studies have been carried out over a non-volcanic hot spring zone consisting of Atri and Tarabalo hot springs along the intracontinental Mahanadi rift basin to delineate the subsurface structures and to understand their effect on the geothermal activities over a stable continental region. Calculated gravity and magnetic anomaly maps unveil the presence of hot springs along Mahanadi fault. The four-layer subsurface configuration as observed using radially averaged power spectrum analysis and 3D Euler solutions of both gravity and magnetic data indicates occurrence of multi-phases sedimentation and tectonic events. 2D forward, 2D inverse, and 3D inverse residual gravity models have delineated high-density igneous intrusive bodies surrounded by comparatively less dense Khondalites and Charnockites rich altered zones. The sharp high to low density transition zones are identified as the regional Mahanadi fault. The India–Antarctica rifting, existence of two hot springs along the Mahanadi fault of the rifted basin, and similarity in water chemistry strongly indicates an interconnection between these two hot springs. Igneous intrusions and radiogenic element-rich metamorphosed shallow formations combinedly acting as the heat source. Deciphered altered zone, deeper intrusion and deeply connected regional fault along the hot springs confirmed that this regional fault is providing the major pathway for water circulation through radioactive element-rich altered zones while the local and shallow fractures connecting the Mahanadi fault feed the hot springs of the study area.
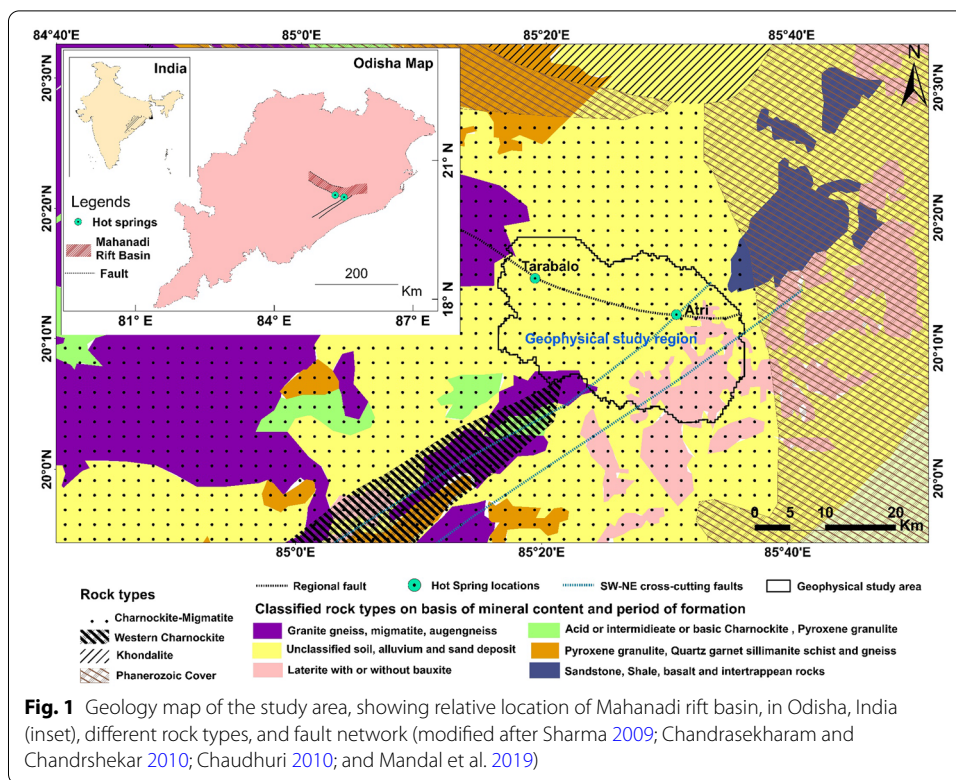
Keywords: Mahanadi basin, Hot springs, Igneous intrusions, Gravity–magnetic, 2D and 3D model

Introduction

Rifts commonly associate with stretching and thinning of the crust, formation of sedimentary basin along with mantle upwelling and melting (McKenzie 1978; Morgan 1983; Lysak 1992; Cloetingh et al. 2013; Koptev et al. 2015). As a result, the rift system and its

adjacent areas are often associated with high heat flow and are more prone to depict hydrothermal activities (Lysak 1987). Intracontinental rifts within tectonically active regions are generally related to high geothermal activities due to volcanism, for examples, the East-African rift system and Lake Baikal (Lysak 1987; Friedmann and Burbank 1995; Njinju et al. 2019; Elizondo et al. 2021). High-frequency geothermal activities due to magmatism are also observed along different plate boundaries, like the East Pacific Rise (Spiess et al. 1980), the Champagne hot spring in Dominica (McCarthy et al. 2005) and the hot springs in the Taupo Volcanic Zone in New Zealand (Hochstein 1995). On the other hand, there exist some hot springs within intracontinental rifted basins but inside present-day stable continental regions, like Fang hot springs of northern Thailand (Wood et al. 2018), Rhine rift basin of Central Europe (Bachler et al. 2003) and Dholera hot spring of India (Sircar et al. 2015). The key factor that governs the geothermal activity in any such region is the abundant heat supply from a deep-seated magmatic source and a permeable stratum for water circulation (Gupta and Roy 2007) while the radioactive elements in the upper crustal rocks may account for the local thermal anomalies (Hasterok and Webb 2017). These thermal anomalies are evident with surface manifestation as hot springs with hydrothermal fluid convection along permeable multiscale fracture/fault system. Therefore, it can be summarised that geothermal activity in rifted, but nowadays stable environments are often associated with past tectonic activities with minuscule contribution from radiogenic heat of the subsurface rocks (Lysak 1987, 1992; Njinju et al. 2019).

The Mahanadi rift basin in Indian Shield accounts for one such intracontinental rift system parallel to Eastern Ghats Mobile Belt (EGMB) (Lisker and Fachmann 2001; Lisker 2004) with hot springs located along the southern flank of the basin. The rift basin being a part of Gondwana basin inherited complex geological processes of faulting, folding, and rifting during the formation of Gondwana master basin (Veevers and Tewari 1995). Researcher have associated the evolution of the basin and its complex rift system either with formation of Lambert rift, Antarctica (Hofmann 1996; Fedorov et al. 1982; Lisker and Fachmann 2001; Lisker 2004) or a multiphase rifting of Son lineament known as Son–Mahanadi rifting (Choudhary 1979). However, the proposed model which depicts that the Mahanadi rift basin is a result of intra-Gondwana rifting in the India–Antarctica sector is supported by various paleontological, stratigraphic and structural observations (Fedorov et al. 1982; Lisker and Fachmann 2001; Bose et al. 2020). Numerous observations including crustal thickness, sedimentation pattern, architecture of metamorphic basement, kinematics and paleo-current indications revealed striking similarity between both Mahanadi and Lambert rift (Hofmann 1996; Lisker and Fachmann 2001). These tectonic activities along with the drag between India and Antarctica may have resulted in series of secondary effects like shearing along the basin, metamorphism of the crustal rocks, geothermal activities, etc. One of the major secondary effects of these cretaceous tectonic activities may be the development of hot springs in the southern flank of the Mahanadi rift basin, i.e., Atri and Tarabalo hot springs along the Mahanadi fault (Fig. 1). The detailed investigation of subsurface structure beneath such hot springs can help in understanding geothermal system in a non-volcanic and present-day tectonically inactive region.

Fig. 1 Geology map of the study area, showing relative location of Mahanadi rift basin, in Odisha, India (inset), different rock types, and fault network (modified after Sharma 2009; Chandrasekharam and Chandrshekar 2010; Chaudhuri 2010; and Mandal et al. 2019)

A few researchers have also tried to understand the subsurface configuration of the Mahanadi basin including the hot springs areas using geophysical observations. The regional scale gravimetric study of the basin by Mishra et al. (1999) revealed a thinner crust with a high-density (3000 kg/m^3) lower part underplating beneath a comparatively low-density (2650 kg/m^3) upper part. The study also depicted variation of thickness of the high- and low-density bodies in the upper crust from place to place depending on sedimentation. Evidence of magmatic underplating was also inferred from seismic observation in the Mahanadi delta region (Behera et al. 2004). Apart from these regional studies, a few localised geophysical and geochemical studies have been carried out around the two hot springs. Baranwal and Sharma (2006) have depicted the presence of subsurface faulting at Tarabalo hot spring region using magnetic, very low frequency electromagnetic and resistivity sounding data. Mandal et al. (2019) also attempted to delineate the shallow subsurface features using a localised magnetic, 2D resistivity tomography and very low frequency electromagnetic data. This study inferred that the Tarabalo hot spring is fed by highly fractured network while a localised fault might be feeding the Atri hot spring, but the exact depth of the source, probable deeper connectivity and subsurface configuration could not be revealed. Maitra et al. (2020) suggested that the hot springs are surface manifestation of localised hot water pockets heated by some radiogenic sources. Based on geochemical and geophysical investigations, they inferred that the radioactive mineral-rich lithologies near the vicinity of the hot springs act as source for such isolated thermal pockets. Although these radioactive rocks account for heat generation of > 2.5 μ Wm^{-3}, a considerably higher average surface heat flow (~ 76 m Wm^{-2}) of Mahanadi basin region as reported by previous studies (Rao

and Rao 1983; Sarkar and Saha 2006) contradicts the concept of anomalous pockets of thorium-rich rocks as the only source of geothermal heat in this region. In addition, the similarity in surface temperature, stable isotope ratios, and ionic concentration of the hot waters from these hot springs (Zimik et al. 2017; Maitra et al. 2020) situated along the same Mahanadi fault do not support the concept of isolated thermal pockets. As a result, the nature of source and detailed subsurface configuration of the geothermal system of this region remains uncertain and a detailed geophysical investigation of this rift basin is indispensable.

In the present study, an effort has been made to decipher the crustal configuration of the region surrounding Atri and Tarabalo hot springs using gravity and magnetic data. The investigation of structural setup around the study area was accomplished by the open-source regional gravity anomaly data while the acquired land gravity–magnetic data serve the purpose to image crustal configuration beneath the hot springs. The faulted plane and metamorphosed zones were delineated using depth estimation techniques, and 2D/3D subsurface modelling (forward and inverse) of the land gravity data sets of the region. Based on the structural inferences from gravity and magnetic data sets, a probable schematic representation of the tectonic model is discussed to better understand the hot spring area parallel to the Mahanadi rift basin. The integrated geophysical investigations infer the presence of deeper igneous underplating with different sill and dike like features, which might act as the primary heat source for the hot springs in this region while a minuscule contribution may have come from the radiogenic elements of the shallow surface metamorphosed rocks. Heat from the source gets transferred convectively through the successive layers and raises the temperature of the meteoric water stored in the pore space and fractures zone of the subsurface rocks. The study infers that the two hot springs (i.e., Atri and Tarabalo) are connected through deep-seated regional fault (i.e., Mahanadi fault) and the hot water is circulated though some of the local and shallow faults or fissures connected to this main deep-seated regional fault.

Geological setting

The study area lies in the central part of the Eastern Ghats Mobile Belt (EGMB) along the NW–SE trending Mahanadi fault in the southern flank of Mahanadi rift basin consisting of two hot springs, namely, Atri and Tarabalo situated ~ 21 km apart (Fig. 1).

Mahanadi rift basin

Present-day Mahanadi rift basin and the Eastern Ghats Mobile Belt (EGMB) are largely shaped by different orogenic activities and sedimentation process starting from Precambrian period (Veevers and Tewari 1995; Lisker and Fachmann 2001; Bose et al. 2020). The Mahanadi rift basin being a part of the Gondwana master basin has been subjected to the huge sedimentations during Carboniferous, Permian, Triassic and Early Jurassic periods that are overlaid on Archean and Proterozoic basement rocks (Lisker and Fachmann 2001). Around 600 km long Mahanadi basin extends from the passive eastern continental margin of India in the SE to the Narmada Son valley in the NW (Lisker 2004) and inherits part of East-Indian geothermal province (Baranwal and Sharma 2006; Yadav and Sircar 2020). The Kerajung Fault and Mahanadi Fault are inferred to be the northern and southern bounds of the rift basin, respectively (Bose and Gupta 2018). Both the

faults have dextral strike slip movements with the former being ~ 150 Ma younger than the latter (Veevers and Tewari 1995) (Fig. 1). The study area is confined to ~ 544 km² area around the two hot springs (namely, Atri and Tarabalo) of East-Indian geothermal province along the NW–SE trending Mahanadi fault (Fig. 1). Apart from the Mahanadi fault, SW–NE trending faults crosscut it towards the south-west portion of the study area (Chandrasekharam and Chandrshekar 2010) (Fig. 1). The study area also consists of various litho-units of metamorphic and sedimentary origin (Baranwal and Sharma 2006; Zimik et al. 2017; Mandal et al. 2019; Maitra et al. 2020) (Fig. 1). It mainly consists of high-grade metamorphic gneisses, i.e., Khondalites (garnet–sillimanite gneisses) and Charnockites (hypersthene bearing granites). In some regions, megacrystic gneisses and quartzo-feldspathic gneisses are found in association with metasedimentary rocks. However, the region is predominantly covered by quaternary sediments with very few noticeable geological exposures within 50–60 km radius about the hot springs. These outcrops show intrusive mafic dikes related to continental rifting phase (Bhattacharya et al. 2010) and highly folded terrain in some regions. Heat flow data of the region also show considerably higher values (> 70 m W/m²) compared to the other stable cratonic regions (Rao and Rao 1983; Sarkar and Saha 2006).

Local geological setup and characteristics of the hot springs

The hot spring at Atri (20°12′24.28″N, 85°30′47.91″E) consists of a single spout and is situated in the eastern part of Khurdha district of Odisha. However, several spouts are observed over a 0.01 km² marshy area (Baranwal and Sharma 2006) at Tarabalo (20°15′4.68″N, 85°19′15.57″E) located in the northern part of Nayagarh district of Odisha. The surface temperature of the thermal springs ranges from 55 to 60 °C (Chandrasekharam and Chandrshekar 2010). Lateritic uplands, alluvial plains and hilly terrain are the major physiographic units observed in the vicinity of the region. Khondalite, Charnockite (Precambrian) and alluvium (Quaternary) are the predominant geological formations of these regions (Central Ground Water Board, Govt. of India 2013a, b). Charnockites are well mapped due to its abundance in the outcrops while Khondalites are rarely present in the outcrops around the hot springs. Geochemical evaluation of the water samples from both Atri and Tarabalo hot springs shows striking similarities in terms of pH range, ionic concentration, and stable isotopic ratios (Zimik et al. 2017; Maitra et al. 2020). A mutual connection through deep-seated fractures along the Mahanadi fault that may act as a channel to feed the hot springs cannot be nullified due to these striking isotopic similarities, proximity, and common geological association between these two hot springs. As a result, exploring the deeper geological features in combination with developing a clear understanding about the evolution of this region is very important.

Methodology

In the present study, open-source regional gravity and acquired land gravity–magnetic data sets were utilised to understand the subsurface geological configuration of the Mahanadi rift region around the Atri and Tarabalo hot springs.

Geophysical data

The large-scale mapping of the gravity signatures was done using publicly available free air gravity anomaly and elevation data of the Mahanadi basin area from the TOPEX data sets (ftp://topex.ucsd.edu/pub; Smith and Sandwell 1997; Sandwell et al. 2014). A detailed subsurface investigation was also performed by acquiring a total of 1876 gravity and magnetic points over ~ 544 km^2 area around the two hot springs using a CG6 gravimeter (with resolution 0.001 mGal) and a GSM-19 T proton precession magnetometer (with resolution 0.01 nT), respectively. The station spacing was varied between 300 and 500 m depending on the accessibility.

Gravity

The publicly available free-air anomaly data of TOPEX were corrected for Bouguer slab and terrain effects considering the average crustal density as 2670 kg/m^3 to obtain the complete Bouguer anomaly map for the Mahanadi rift region (Fig. 2). The Bouguer gravity signature of Mahanadi basin was utilised to properly investigate the regional tectonic features of the study area.

The acquired land gravity data were corrected by removing the instrument drift, tidal and topographic effects. The drift-corrected gravity values were tied with a local base station as established at Public Works Department office Khurdha (20.180759°, 85.618210°) with respect to a known base station at Jajpur–Keonjhar road railway station
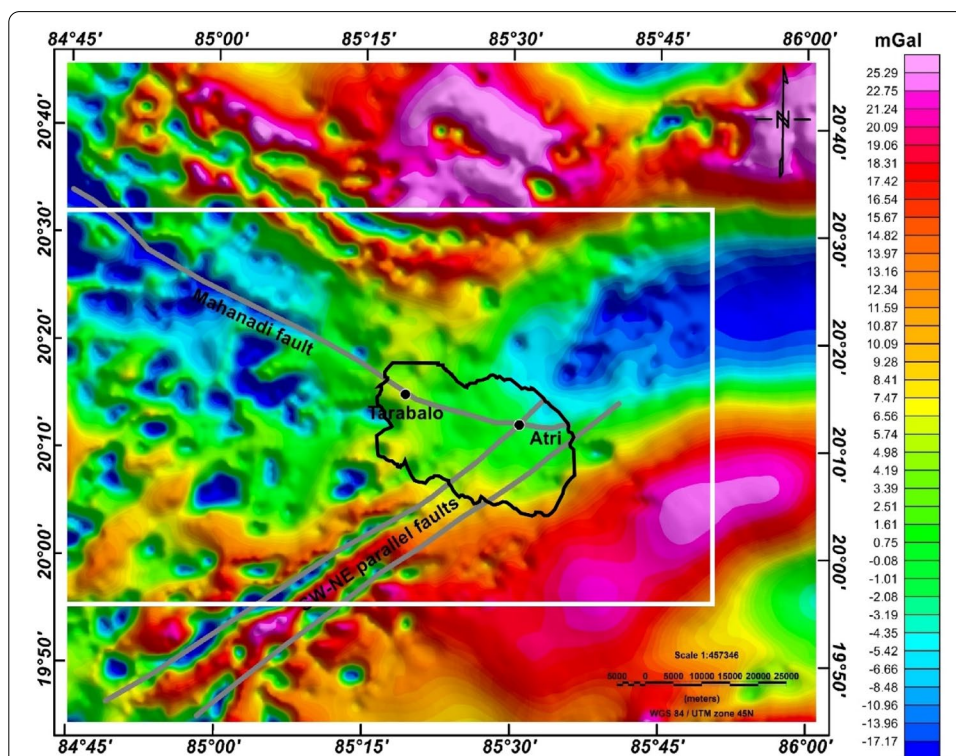

Fig. 2 Bouguer anomaly over wider region along Mahanadi rift basin based on the open- source TOPEX data sets. The black polygonal feature surrounding the hot springs denotes the region covered by land geophysical survey while grey lines show faults in the region and the white square represents the outline of the area covered by the Geology map (Fig. 1)

(absolute reading $=978,706.46$ mGal) (Qureshy et al. 1973). The theoretical gravity value at each location was calculated using Geodetic Reference System 1967 (GRS67). Free-air correction term was calculated by the standard free-air gradient of 0.3086 mGal/m. To compute the Bouguer correction, an average crustal density of 2670 kg/m^3 was assumed. Digital elevation model was created from the acquired differential global positioning system data and was used for topographic correction. The elevation of the study area varied from ~ 22 to ~ 105 m and corresponding maximum terrain reduction value is ~ 0.2803 mGal. The calculated Bouguer anomaly values are presented as contour map using minimum curvature gridding technique in Geosoft software (Fig. 3a). The Bouguer anomaly obtained after implementing the above corrections was subjected to regional and residual separation using the interactive filter module of Geosoft software. In the present study, Gaussian low-pass filter with a cut-off wavelength of 10,000 m was implemented based on trial-and-error approach to filter out the deeper features (Fig. 3b). Finally, the residual gravity anomaly was recovered by subtracting the obtained regional gravity anomaly values from the Bouguer anomaly values (Fig. 3c).

Magnetic

The acquired ground magnetic data were subjected to diurnal and International Geomagnetic Reference Field (IGRF) corrections to get the total magnetic field (TMF) anomaly values which are then presented as a contour map using minimum curvature gridding technique in Geosoft software (Fig. 4a). The bipolar distortions (Baranov 1957; Roest and Pilkington 1993) in magnetic anomalies are generally eliminated by applying reduce-to-pole (RTP) or reduce-to-equator (RTE) transformation. However, RTE is preferred over RTP in the mid- and lower latitude areas (Jain 1988). Therefore, the total field magnetic anomaly data were further corrected by applying RTE transformation in Geosoft software and using the average inclination and declination values of the study area are as 29.663° and -0.345°, respectively (Fig. 4b).

Depth estimation techniques

Two depth estimation techniques, namely, 3D Euler deconvolution and radially average power spectral analysis were further employed on the calculated gravity and magnetic anomalies for understanding the subsurface configuration of the region. Based on the available geological knowledge and derived layering configuration, 2D forward as well as 2D and 3D inverse modelling were also performed on the residual gravity anomaly data to delineate the lateral and vertical continuity of the identified anomaly zones adjacent to the hot springs.

Euler depth solutions

The depth and location of an anomalous target body can effectively be traced out by employing Euler deconvolution technique based on Euler's homogeneity equation (Thompson 1982). In the present investigation, 3D Euler technique (Reid et al. 1990) was implemented on residual Bouguer and reduced to equator (RTE) anomaly of gravity and magnetic data sets, respectively. The following 3D Euler equation was solved for tracing out the locations and depths (x_0, y_0, z_0) of the respective anomalous sources:
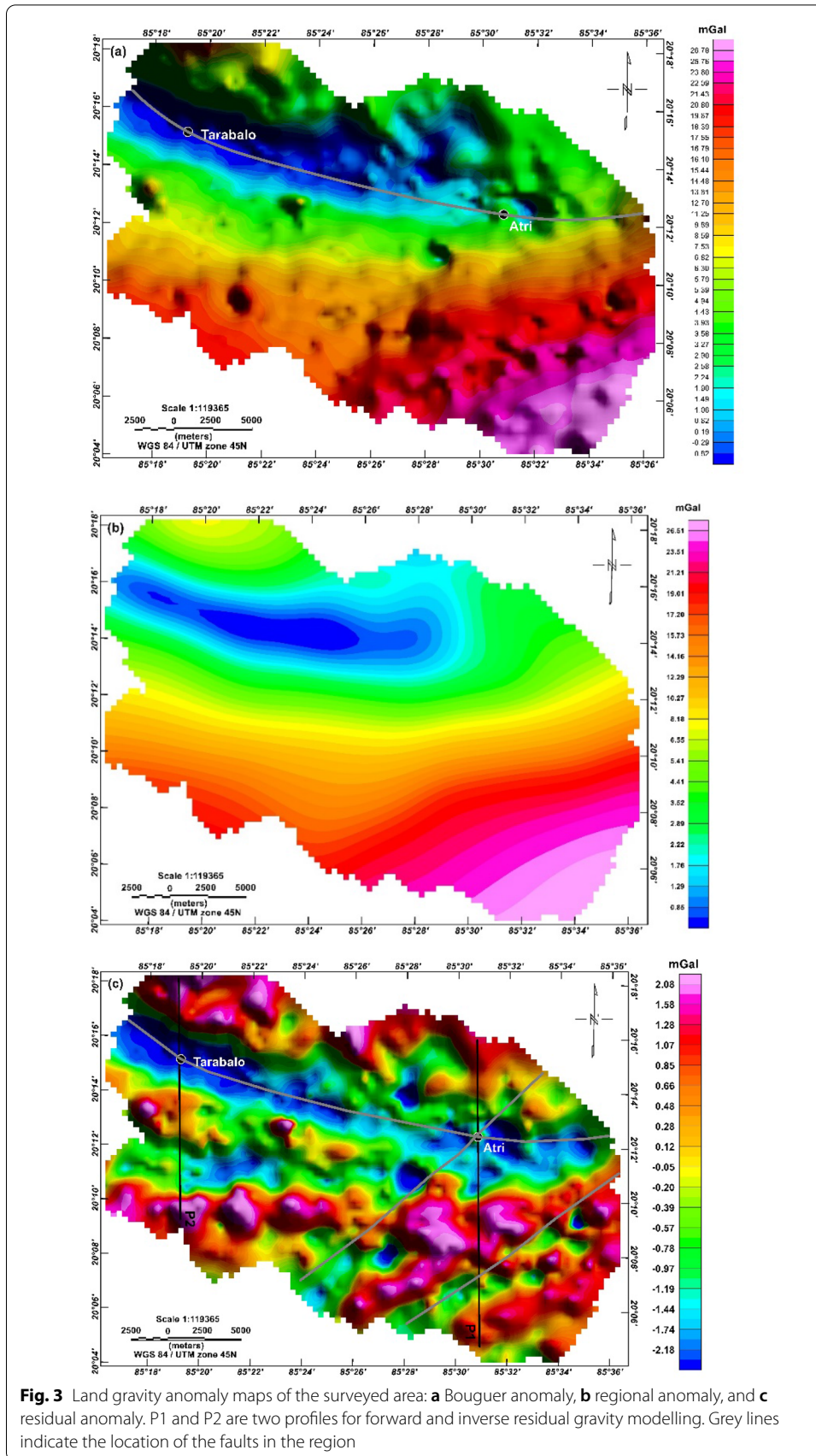
Fig. 3 Land gravity anomaly maps of the surveyed area: **a** Bouguer anomaly, **b** regional anomaly, and **c** residual anomaly. P1 and P2 are two profiles for forward and inverse residual gravity modelling. Grey lines indicate the location of the faults in the region

Fig. 4 Magnetic anomaly maps of the surveyed area: **a** total magnetic field (TMF) anomaly, and **b** reduced to equator (RTE) anomaly. Grey lines indicate the location of the faults in the region
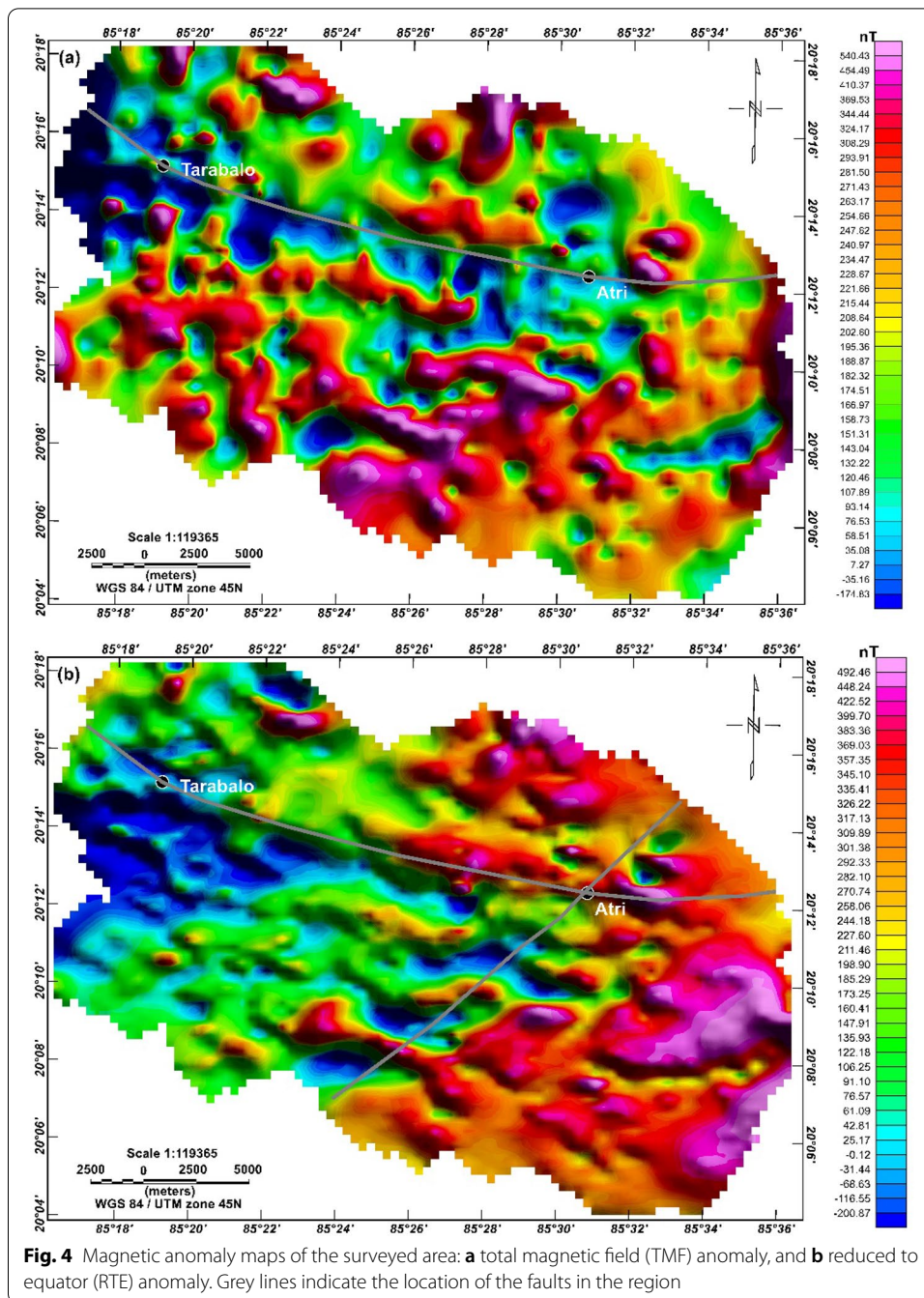
$$(x - x_0)\frac{\partial f}{\partial x} + (y - y_0)\frac{\partial f}{\partial y} + (z - z_o)\frac{\partial f}{\partial z} = -N(B - f), \tag{1}$$

where f is the observed potential field (gravity or magnetic) at (x, y, z) [coordinates of the grid nodes], B is the base level of the field (i.e., the regional value at (x, y, z)] and N is the Euler's structural index (SI) (degree of homogeneity) whose value depends on the geometry of the source body (Reid et al. 1990; Mandal et al. 2020; Yadav and Sircar 2021). Fast Fourier transform (FFT) was used to calculate the gradients along three orthogonal

axes. In case of magnetic data, this technique is more accurate than gravity as the solutions image the top corner of the structure in magnetic while in gravity it accounts for deeper level corresponding to the centre of mass (Fairhead 2015). Owing to the bipolar nature of the magnetic field, the structural index values are different for magnetic and gravity anomaly, i.e., for fault SI = 1 for gravity but SI = 2 for magnetic (Reid et al. 1990). In the present study, presuming a faulted and layered subsurface, the SI was assumed to be 1 and 2 for gravity and magnetic anomalies, respectively. A set of equations were solved at each grid point within a judicially chosen window to reduce the effect of multiple sources but covering substantial field variations (Mandal et al. 2020). In the present study, with a depth tolerance of 15% and window size of 10 grid cells, the Euler depth solutions were calculated using the Geosoft software (Fig. 5a, b).

Radially averaged power spectrum

Two-dimensional radially averaged power spectrum analysis of the potential field data is one of the commonly used techniques for estimating depth of anomalous sources (Bhattacharya 1966; Spector and Grant 1970). The technique relies on spectral analysis of gravity–magnetic data sets in Fourier domain. Radially averaged power spectrum of residual Bouguer gravity and RTE magnetic anomaly data were calculated using Fast Fourier transform. The natural logarithm of power of the respective anomaly data was calculated and plotted against the wavenumber. The plot was divided into several straight-line segments including a set of collinear points in each segment. In the present study, the first set of collinear points was chosen to be the power spectrum component corresponding to the wave numbers for the deepest layer. Other successive straight-line segments with increasing frequency (i.e., decreasing slope) were chosen for different layers. Dividing the slope of each straight line with 4π gives the depth (h) of successive anomalous layer as:

$$h = \frac{P(k_1) - P(k_2)}{4\pi(k_1 - k_2)}, \tag{2}$$

where k_1 and k_2 are start and end points of radial frequencies and $P(k_1)$ and $P(k_2)$ are the corresponding values of radially averaged power spectrum component (Spector and Grant 1970; Guo et al. 2013). Figure 6a, b shows the 2D radially averaged power spectra analysis of gravity and magnetic data sets using the radial average power spectrum module of Geosoft software.

2D and 3D gravity modelling

The 2D forward and inverse modelling of the residual gravity anomaly along two NS profiles passing through the Atri and Tarabalo hot springs and 3D inverse modelling were carried out using a prior knowledge about the local geology and different layering information as obtained from the radial power spectra of the gravity data. In the present study, GM-SYS module of Geosoft software was used for 2D forward modelling and a MATLAB based 2D and 3D improved compact inversion approaches were employed for inverse modelling (Srivastava et al. 2018). 2D gravity model of GM-SYS module calculates the cumulative gravity effect of polygonal features using the solutions of Talwani et al. (1959) and Won and Bevis (1987).
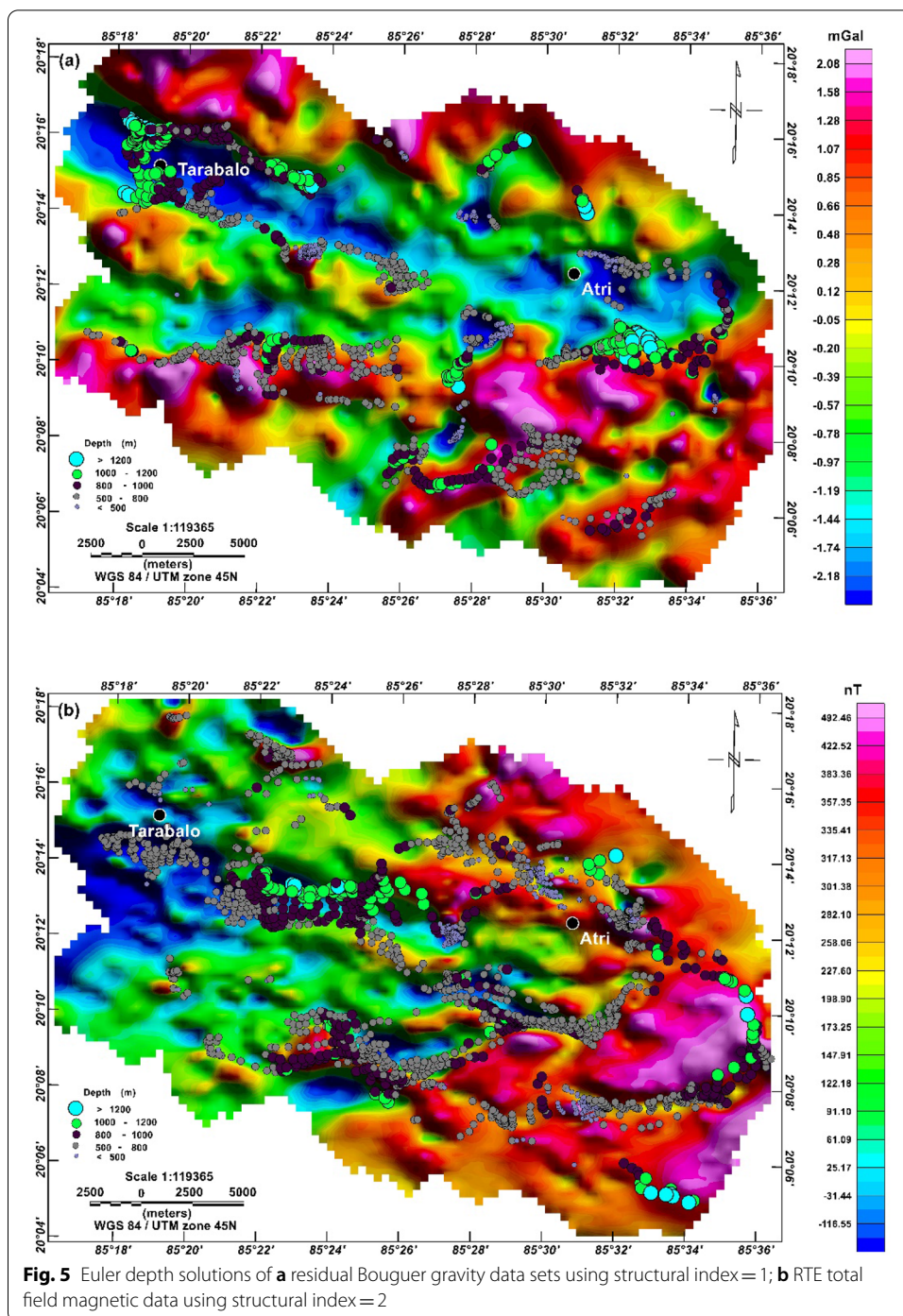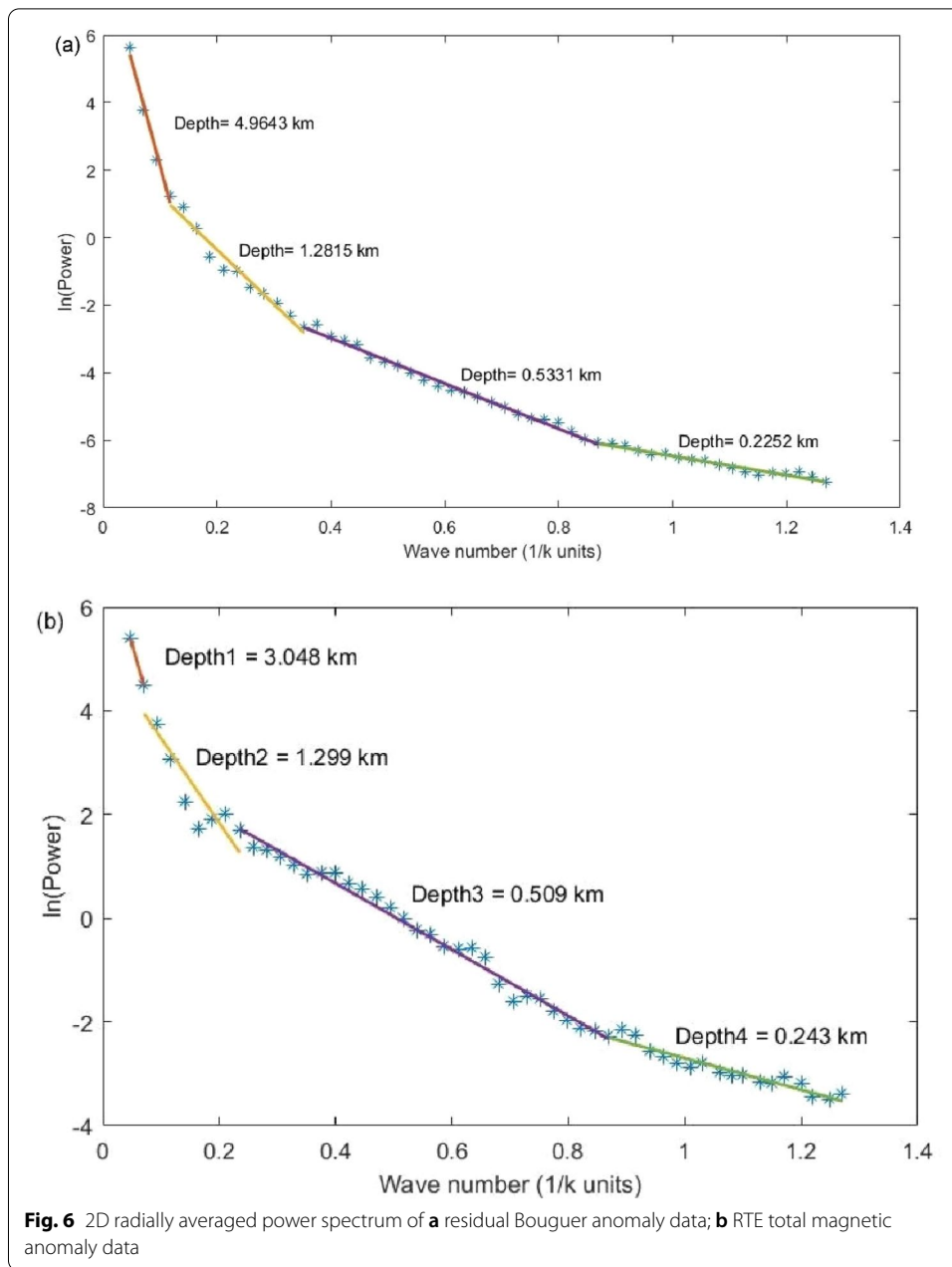
Fig. 5 Euler depth solutions of **a** residual Bouguer gravity data sets using structural index = 1; **b** RTE total field magnetic data using structural index = 2

The improved compact inversion modelling is a weighted least square-based inversion scheme to decipher shape and depth of the anomalous mass distribution. The modelling was carried out by dividing the subsurface into combination of right rectangular blocks (for 2D) and cuboidal prisms (for 3D), whose densities were allowed to vary both laterally and vertically. The inversion method satisfies a general linear equation:

Fig. 6 2D radially averaged power spectrum of **a** residual Bouguer anomaly data; **b** RTE total magnetic anomaly data

$$g_{\mathrm{obs}} = \sum_{1}^{M} A_{ij} m_j, \tag{3}$$

where g_{obs} is $(N \times 1)$ gravity anomaly vector, m is $(M \times 1)$ density vector, and A $(N \times M)$ is the kernel matrix. The kernel matrix consists of $N \times M$ number of elements and quantifies the contribution of jth cell to the ith observation point. The inversion method iteratively solves Eq. (3) for model parameter m using the weighted least square approach. For kth iteration, the updated solutions were given as (Srivastava et al. 2018; Mandal et al. 2013):

$$m^{k+1} = 0.95m^k + W_{m(k)}^{-1}A^{\mathrm{T}} \times \left[A W_{m(k)}^{-1}A^{\mathrm{T}} + \varepsilon_0^2 W_{e(k)}^{-1}\right]^{-1}\left[g_{\mathrm{obs}} - Am^k\right], \qquad (4)$$

where W_m and W_e are the model weighing and error weighing matrix, respectively, and ε_0 is the damping factor (regularisation parameter) to get rid of matrix singularity. The damping factor can vary from 0.01 to 1.21 depending on the noise level of the data points. In the present study, the damping factor is chosen to be 1.21 based on several trials. Local geological information indicates the presence of high-density metamorphosed rock overlain by layers of sedimentary formations (Central Ground Water Board, Govt. of India 2013a, b; Behera et al. 2004). Therefore, the density bound with a minimum of 2000 kg/m^3 to a maximum of 2800 kg/m^3 has been chosen to recover an approximate density model of the subsurface.

Results

Gravity and magnetic anomaly maps

Gravity

The Bouguer anomaly map of Mahanadi basin (Fig. 2) shows a wide variation in gravity values (-13.96 to 25.29 mGal). A NW–SE trending low-gravity (-13.96 to -5.42 mGal) zone in the western part is observed to be broadened and changed its trend to nearly EW while approaching towards eastern part of the study area. The southern flank of this low-gravity zone is inferred to be the Mahanadi fault (marked by grey line in Fig. 2) while the broad gravity low in the east is inferred to be part of Mahanadi rift basin. Apart from the prominent rifted basin two much-pronounced SW–NE trending gravity lows are observed to be cutting across the Mahanadi rift basin approximately at 20° 10′ N and 85° 30′ E. More pronounced gravity high (13.97–25.29 mGal) toward north, north-east corner and south-east corner of the Bouguer anomaly map may be due to the presence of granulites, Charnockites and Khondalites (see Figs. 1 and 2). Khondalites are formed due to metamorphism of sedimentary rocks (Gogte and Ramana 1976) while the granulite and Charnockite are the metamorphosed form of igneous rocks (Dasgupta et al. 2013). Therefore, the zones with moderate–high gravity anomaly may be associated with less dense Khondalites while that with high amplitude of gravity anomaly may be due to the present of high-density rocks, like granulite and Charnockite (see Figs. 1 and 2). The considerable changes in amplitude of gravity highs and lows are observed due to variation in sediment thickness and presence of different types of metamorphosed rocks (Figs. 1 and 2). This regional variation in rock formations and existence of faulted network indicate that the region has undergone high degree of alteration and sedimentation process in due course of tectonic events.

The Bouguer anomaly map (Fig. 3a) as generated from the acquired land gravity data deciphered relatively high gravity anomaly toward south and south-eastern parts of the study area with a maximum magnitude of $\sim +26.78$ mGal and minimum of $\sim +5.70$ mGal. Overall, low-gravity anomaly values between -0.29 and $+5.39$ mGal are observed around Atri and Tarabalo hot spring zones (Fig. 3a). The NW–SE and W–E trending low anomaly zone over the hot spring locations can be interpreted as Mahanadi sub-basin nearly parallel to the Mahanadi fault (Figs. 1 and 3a). The residual gravity map obtained after filtering out the regional effects (Fig. 3b) was found to be more informative about the shallow surface features (Fig. 3c). Along with the NW–SE trending

low anomaly zone, one W–E trending low anomaly zone at the middle and few SW–NE trending low anomaly zones at the southern part of the study area are observed in the residual gravity anomaly map (Fig. 3c). The steep decline in gravity values from high (+2.08 mGal) to low (−2.18 mGal) at the northern flank of the NW–SE low anomaly zone can be inferred as the Mahanadi fault (see Figs. 1, 2 and 3c). The high residual anomaly (~0.85–2.08 mGal) zones in the anomaly map might be due to the presence of highly metamorphosed rocks, like Khondalites, Charnockites or granitic gneiss while the low-to-moderate anomaly (−0.39 to +0.28 mGal) zones may be caused by the presence of quaternary sediments and the weathered Khondalites or Lateritic rocks, respectively (Figs. 1 and 3c).

Magnetic

The total magnetic field (TMF) anomaly map of the study area deciphered several high and low anomaly linear patches along with a prominent NW–SE trending low anomaly zone (Fig. 4a) co-relatable with the NW–SE trending low anomaly zone of the residual gravity map (Figs. 3c and 4a). In the present study, the magnetic anomaly map was further enhanced by applying reducing to equator (RTE) transformation that shows a broad high anomaly (227.60–492.46 nT) towards SEE and a broad low (−116.55 to 61.09 nT) towards NWW (Fig. 4b). A linear NW–SE trending high-to-low transition zone adjacent to the hot springs reveals good correlation with the NW–SE trending low of residual gravity zone (Figs. 4b and 3c). The predominance of high towards eastern region in comparison to the north-western region can be inferred as the presence of comparatively high susceptibility rock like Granitic gneiss in the eastern region while low susceptibility rock like Khondalites in the western region (Figs. 1 and 4b).

Depth estimation

The Euler depth solutions for identifying the depth extent of faults and fractures were calculated assuming SI as 1 (for gravity) and 2 (for magnetic) which were plotted on the residual gravity and RTE magnetic anomaly maps (Fig. 5a, b), respectively. The depth solutions with depth > 1000 m were observed to be accumulating along the NW–SE trending low zone in the residual gravity and RTE magnetic maps. This observation indicates that the NW–SE trending low anomaly zone related to the regional fault might be extending beyond 1000 m depth (Fig. 5a, b). A wide variation of depth solutions from 500 to 800 m in both gravity and magnetic data may be related to the depth extent of the shallow faults and fractures beneath the quaternary sediments. The radially averaged power spectrum analysis of residual gravity and reduced to equator magnetic data indicates four depth interfaces at ~3050–4950, 1300, 500, and 230 m approximately (Fig. 6a, b).

2D and 3D gravity model

2D forward and inverse modelling along two NS profiles P1 and P2 passing through the Atri and Tarabalo hot springs, respectively, were carried out using four-layer configuration. Depth of interfaces were assumed at 300, 500, 2000, and 5000 m from the surface by approximately correlating with the depths as obtained from radially averaged power spectrum and Euler depth solutions. The forward model clearly demonstrates a four layered

subsurface with densities 2000, 2400, 2750 and 2800 kg/m^3 from top to the deeper layers, respectively (Fig. 7a, b). In inverse modelling, the layers have been discretised into square blocks of 100×100 m. The density constraints for both forward and inverse model were taken from Mishra et al. (1999) and Behera et al. (2004). The root mean square error for the
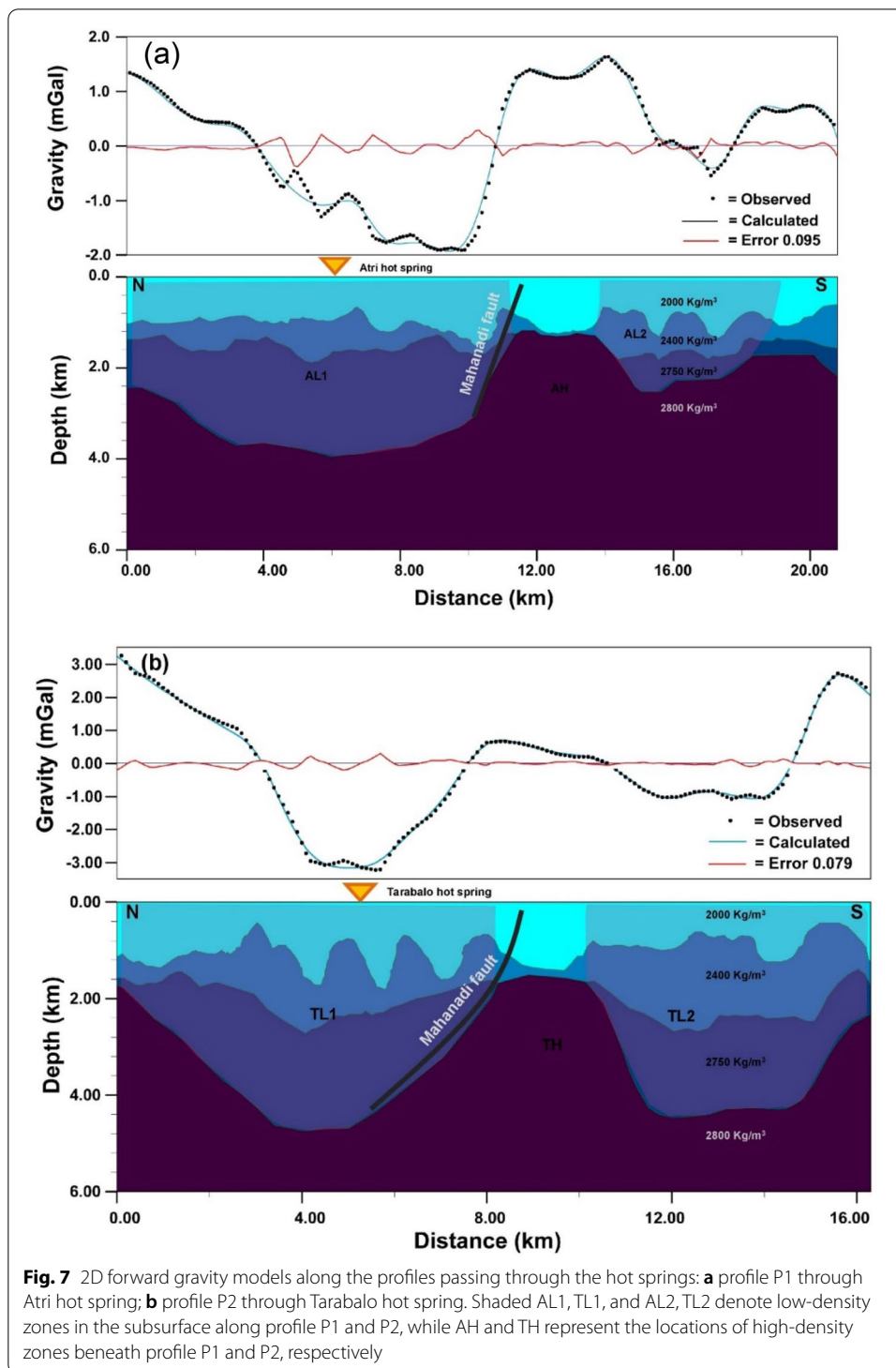

Fig. 7 2D forward gravity models along the profiles passing through the hot springs: **a** profile P1 through Atri hot spring; **b** profile P2 through Tarabalo hot spring. Shaded AL1, TL1, and AL2, TL2 denote low-density zones in the subsurface along profile P1 and P2, while AH and TH represent the locations of high-density zones beneath profile P1 and P2, respectively

forward models (Fig. 7a, b) were found to be 0.095 and 0.079 mGal for profiles along Atri (P1) and Tarabalo (P2), respectively, while that of the 2D inverse models (Fig. 8a, b) were observed to be 0.043 and 0.069 mGal, respectively. The inverse models show striking similarity with respect to the low- and high-density spreads in the subsurface of the forward models. The 2D forward and inverse models along the two profiles deciphered a broad high-density zone (AH and TH along P1 and P2 profiles, respectively) sandwiched between two low-density zones (AL1, AL2 and TL1, TL2 along P1 and P2 profiles, respectively) nearly at the centre of the profiles (Figs. 7a, b and 8a, b). Among the two low-density zones, one towards the northern side of the profiles (i.e., AL1 and TL1 along P1 and P2, respectively) is observed to be comparatively broader than the low-density zone at the southern end (i.e., AL2 and TL2 along P1 and P2, respectively) (Figs. 7a, b and 8a, b). The broad low-density zone towards the northern side of both the profiles is suggested to be a part of Mahanadi rift basin and the sharp contact of the low to high density transition at around 11 and 7 km distance along profiles P1 and P2, respectively, is inferred to be the Mahanadi fault. The 3D gravity model also reveals a NW–SE trending low-density zone in depth slice plot (Fig. 9a). This zone is observed to be broadened at ~4 km depth and can be inferred as the regional Mahanadi fault (Fig. 9b, c). Relatively narrower low-density zone between 15 and 18 km (AL2) and 11–16 km (TL2) towards the southern part of both the profiles (Figs. 7a, b and 8a, b) can be inferred as small sub-basin at the intersection of SW–NE trending fault with the NW–SE trending Mahanadi fault (Figs. 1 and 2). Presence of SW–NE trending cross-cutting faults can also be observed by the low-density zones in slice 2 of 3D inverse model (Fig. 9b, c). The high-density (>2750 kg/m^3) regions as observed at around 11–15 km and 8–11 km lengths along the P1 and P2 profiles (i.e., AH and TH, respectively) is found to be sub-parallel to the Mahanadi fault and can be inferred as igneous intrusions while the comparatively low-density (~2700 kg/m^3) regions at the periphery of the high-density regions (i.e. AL1, AL2 and TL1, TL2) are related to high-grade metamorphosed rock (Figs. 8a, b and 9a, c). As the igneous intrusion was found to be having intermediate density between that of igneous and metamorphic rocks, it can be inferred to granitic intrusion. However, the whole region is covered by thick sedimentary layers.

Discussion

Owing to its non-orogenic origin and inherent low-enthalpy nature, the geothermal system along the Mahanadi rift basin is often undermined and less studied. However, in very recent times few geological, geochemical, and geophysical studies (Chandrasekharam and Chandrshekar 2010; Baranwal and Sharma 2006; Zimik et al. 2017; Mandal et al. 2019; Maitra et al. 2020) have been performed in this region but some of the critical aspects, like source, nature of the geothermal system, relation with regional features and subsurface configuration remain uncertain. The existence of Atri and Tarabalo hot springs along Mahanadi fault of the rift basin, and similarity in water chemistry indicate a genetic relationship between these two hot springs. In the present study, an effort has been made to

(See figure on next page.)
Fig. 8 2D compact inversion gravity models along the profiles passing through the hot springs: **a** profile P1 through Atri hot spring; **b** profile P2 through Tarabalo hot spring. Shaded AL1, TL1, and AL2, TL2 denote low-density zones beneath profile P1 and P2, while AH and TH represent the locations of high-density zones beneath profile P1 and P2, respectively
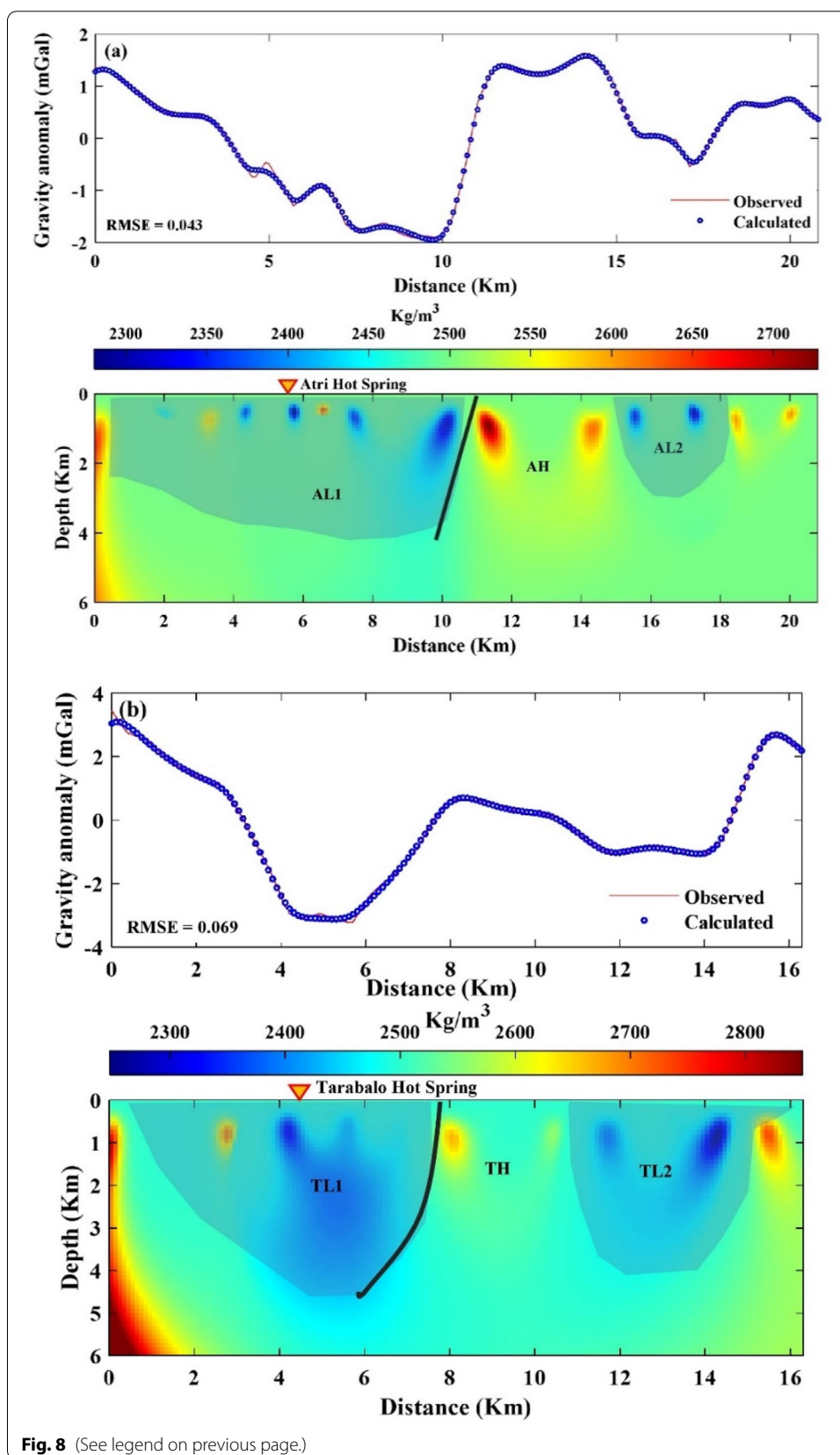
Fig. 8 (See legend on previous page.)

delineate the subsurface structures of the region to understand the source and nature of the geothermal system and its evolution with justified geophysical observations and schematic representations.

Subsurface configurations along Mahanadi rift basin including the hot springs zones

Observations from the wider gravity map along the Mahanadi basin fairly coincides with the observations made from land gravity and magnetic anomaly data (Figs. 2, 3a, c and 4a, b). The Euler depth solutions and 2D as well as 3D gravity models of the hot spring zones effectively delineate the subsurface configuration of the study area (Figs. 5a, b, 7a, b, 8a, b, and 9a, b, c). The two hot springs (i.e., Atri and Tarabalo) were observed to be located along the NW–SE trending Mahanadi fault (Figs. 2, 3a and 4a), while one of the two SW–NE trending cross-cutting fault was observed to be intersecting the Mahanadi fault near to Atri hot spring (Figs. 2, 3c and 4b).

The Euler depth solutions along these faults suggest that the faults might be of deep seated with a depth > 1000 m while the depth solutions between 500 and 800 m depth clustering near the hot springs can be inferred as the depth of local fractures connecting NW–SE and SW–NE trending faults (Fig. 5a, b). Predominance of low-gravity and -magnetic values in the anomaly maps indicate that the region within the Mahanadi rift basin is dominated by low-density and low-susceptibility sediments (Figs. 2, 3a and 4b). Based on the average interface depths as observed from 2D radial power spectrum analysis of gravity-magnetic data and based on the geological affiliation (see Mishra et al. 1999), it can be inferred that the layer above 230 m represents near surface inhomogeneities and recent alluvium, the succeeding layer between 230 and 500 m as quaternary sediments while the layer between 500 and 1300 m depth as the Gondwana sediments. The successive layer to the sediments with depth ranging from 1300 to 4000 m is inferred as high-grade metamorphosed rock while the layer beyond 4000 m can be inferred as igneous rocks (Fig. 6a, b). These igneous rocks are also identified from 2D gravity models and suggested to be intrusive rocks and may be formed by the magmatic activity during India–Antarctica rifting phase. The igneous intrusions can be correlated with the magmatic emplacements and sill type features (known as underplating) as observed by Behera et al. (2004).

The 2D forward and inverse gravity models along the NS profiles across Atri and Tarabalo hot spring zones deciphered the existence of broad high-density mass between two low-density bodies (Figs. 7a, b and 8a, b). The high-density zones (AH and TH) (> 2750 kg/m^3) along profile P1 and P2, respectively, correlated well with the W–E trending elongated gravity highs as observed in the depth slices of 3D gravity inversion models (Fig. 9b, c) and are inferred to be the igneous intrusions. Comparatively low-density rocks (2700–2650 kg/m^3) surrounding these high-density zones can be related to high-grade metamorphosed Khondalite and Charnockite rocks. Maitra et al. (2020) also confirmed the presence of these rock formations containing thorium-rich monazite and thorite. Behera et al. (2004) also inferred the presence of intrusive igneous formations beneath the metamorphic formations (Khondalite and Charnockite) using seismic and forward gravity model. The sharp

(See figure on next page.)
Fig. 9 3D compact inversion gravity models: **a** NS trending slices at different distances; **b** slices at different depths; **c** NS trending slices superimposed with residual gravity anomaly (Fig. 3c). The grey line towards the north of the slices represents the Mahanadi fault and the grey lines towards the second and third slice of Fig. 9c denote the SW–NE parallel faults
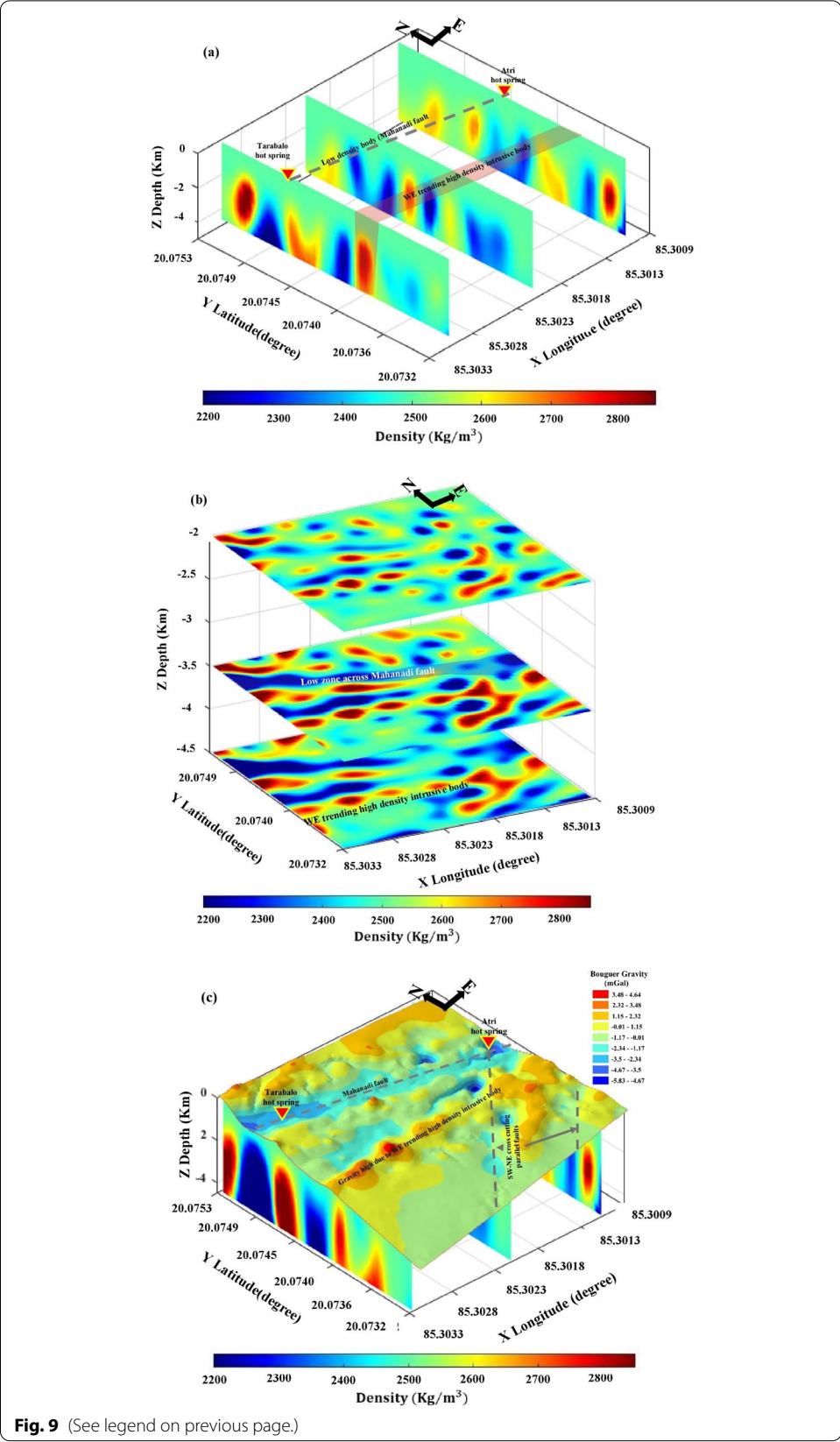
Fig. 9 (See legend on previous page.)

boundary between high- and low-density zone at around 11 and 7 km locations along P1 and P2, respectively, that extending up to 4–5 km depth is identified to be the NW–SE trending regional Mahanadi fault while the broad low zone (AL1 and TL1 along P1 and P2, respectively) near to the fault is the part of Mahanadi rift basin. The Euler depth solutions > 1000 m along with the prominence of the low-density zone in deeper slices of 3D inverse model also confirms the deep-seated nature of the Mahanadi fault (Figs. 5, 9a, b). The faulted subsurface with wide range of density variation ($\sim$2200–2850 kg/m^3) confirms the presence of different rock formations which also indicates that the region has undergone episodic tectonic events with multiphase sedimentation and metamorphism (Fig. 8a, b). History of such episodic tectonic events in this region was also inferred by past researchers (Mishra et al. 1999; Lisker and Fachmann 2001). The 2D and 3D inverse gravity modelling also confirms the presence of the two hot springs in the low-density zone and connected by deep-seated NW–SE trending Mahanadi fault (Figs. 2, 3c, 8a, b, 9a, c and 10). The above observations certainly contradict the isolated anomalous hot pocket theory of Maitra et al. (2020).
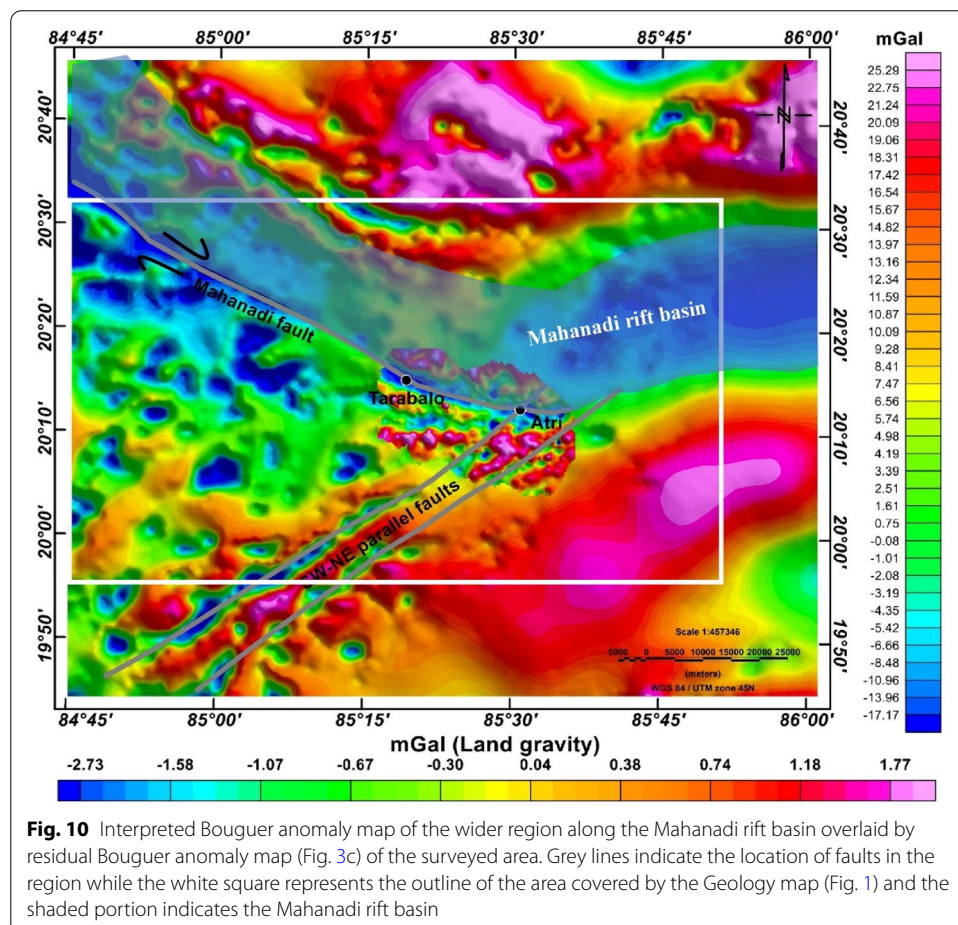

Fig. 10 Interpreted Bouguer anomaly map of the wider region along the Mahanadi rift basin overlaid by residual Bouguer anomaly map (Fig. 3c) of the surveyed area. Grey lines indicate the location of faults in the region while the white square represents the outline of the area covered by the Geology map (Fig. 1) and the shaded portion indicates the Mahanadi rift basin

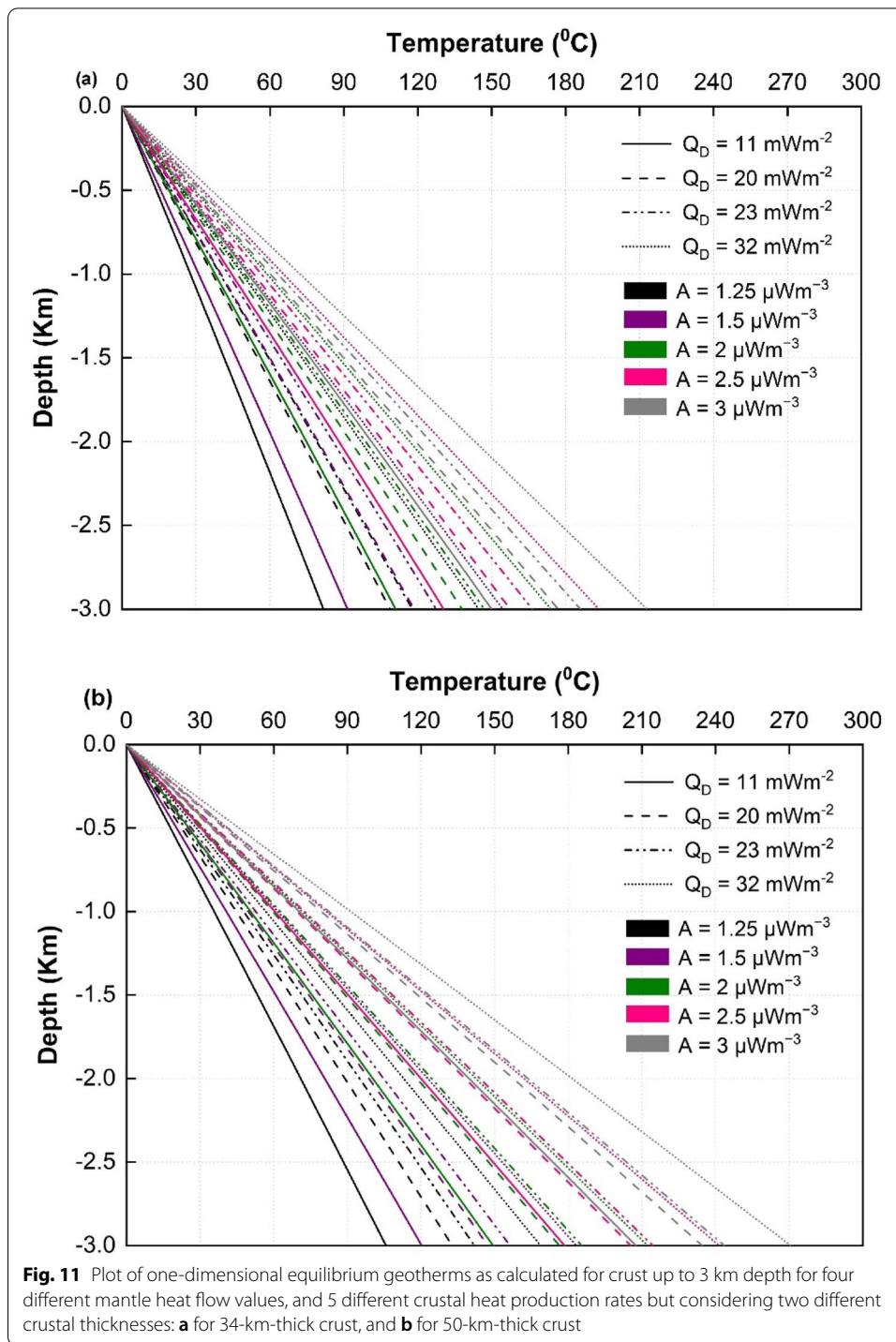### Heat source and the geothermal system

The heat source and connectivity of the thermal water act as key features to understand any geothermal system. Maitra et al. (2020) concluded that the thorium-rich high-grade metamorphosed rocks (Khondalites and Charnockites) of the region are the sole contributor of heat for the hot springs in the region neglecting the contribution of deep seated igneous intrusions. However, it is found that the heat production rate of Khondalites and Charnockites are > 2.5 μ Wm^{-3} (Kumar et al. 2007) is considerably lower than the average surface heat flow of the region, i.e., 76 m Wm^{-2} (Rao and Rao 1983; Sarkar and Saha 2006). Considering equilibrium geotherm for the region, Maitra et al. (2020) showed that the 60 °C isotherm (equivalent to the surface temperature of the hot spring water) can be achieved at a depth as low as ∼ 1 km. However, in their estimation they have assumed the crustal thickness as 50 km which is significantly higher than the average crustal thickness of the region of ∼ 34 km as obtained using global crustal model CRUST 1.0 (Laske et al. 2012) (Table 1). Such a thin crust of the Mahanadi basin area was also inferred by Mishra et al. (1999). Thus, the heat contribution from the crustal sources was overestimated by Maitra et al. (2020) and resulted into elevated crustal isotherms. In the present study, we have recalculated the geothermal gradient using the expression given by Fowler (1990) as:

$$T = -\frac{A}{2k} \times z^2 + \left[\frac{(Q_d + Ad)}{k}\right] \times z, \tag{5}$$

where T is the temperature at depth z below the surface, k is the thermal conductivity of the crust (assumed to be 2.5 Wm^{-1} °C^{-1}), d is the thickness of the crust, Q_d is the

Table 1 Moho depth variation over the study area as calculated by CRUST1.0 model (Laske et al. 2012)

Sl. No.	Longitude (degree)	Longitude (degree)	Moho depth (km)
1	20.5	84	37.87
2	20.5	84.5	37.87
3	20.5	85	36.66
4	20.5	85.5	36.66
5	20.5	86	33
6 (Tarabalo)	20.26	85.31	36.66
7 (Atri)	20.21	85.51	36.66
8	20	84	35.70
9	20	84.5	35.70
10	20	85	32
11	20	85.5	32
12	20	86	26
13	19.5	84	35.70
14	19.5	84.5	35.70
15	19.5	85	32
16	19.5	85.5	32
17	19.5	86	26
Average			34.01

Fig. 11 Plot of one-dimensional equilibrium geotherms as calculated for crust up to 3 km depth for four different mantle heat flow values, and 5 different crustal heat production rates but considering two different crustal thicknesses: **a** for 34-km-thick crust, and **b** for 50-km-thick crust

mantle heat flow, and A is the crustal heat production. We have done these calculations for two different crustal thickness, i.e., 34 and 50 km keeping all other parameters same as Maitra et al. (2020) (Fig. 11a, b). Figure 11a, b shows that the geotherms for 34 km crustal thickness have greater slop than the 50 km thick crust and the 60 °C isotherm for

crustal heat production of 1.25 μ Wm^{-3} can be achieved at a greater depth (~ 2.2 km) than that of 50 km thick crust (~ 1.6 km) for varying crustal heat production. Therefore, the heat flow from deeper crustal layer to the surface cannot be nullified and it can be suggested that thorium-rich rock types, Khondalite and Charnockites might not be the sole contributor to the heat associated with the hot springs. The deep seated igneous intrusions as observed in the density models (inferred to be granitic) may act as the primary heat source with high concentration of heat producing elements (Artemieva et al. 2017) while the Khondalites and Charnockites might have minuscule contribution.

On the other hand, geochemical analyses of the water samples from the two hot springs revealed similarities in terms of pH range, ionic concentration, and stable isotopic ratios (Zimik et al. 2017; Maitra et al. 2020). Based on high concentration of Na, Cl, and fluoride ions in the water samples of both the hot springs, Zimik et al. (2017) also suggested the possibility of deeper circulation of the thermal water through deepseated fault intersecting the granitic terrain of the region. Present geophysical study also confirms the presence of both the hot springs along the deep-seated Mahanadi fault (Figs. 7a, b, 8a, b, 9, and 10), thereby suggesting that the hots springs are connected by the regional fault. Thus, the observations also contradict the idea of isolated hot water pocket as proposed by Maitra et al. (2020). Instead, it is inferred that the shallow surface fractures (< 500–800 m) as observed from the Euler depth solutions (Fig. 5a, b) might act as the pathway between the deep-seated regional fault and the hot spring zones. However, few shallow fractures away from the hot spring regions may not be connected to this deep-seated regional fault thereby give rise to normal water in the tube wells of nearby regions. Figure 12 shows a 3D conceptual model illustrating the subsurface structure beneath the Mahanadi rift basin and describes the hydrothermal circulation along Mahanadi fault. The model depicts that the deeper igneous bodies are the primary heat source for the hot springs. The convectional heat circulation between the successive layers of metamorphic (Khondalite and Charnockite) and igneous formations transfer the
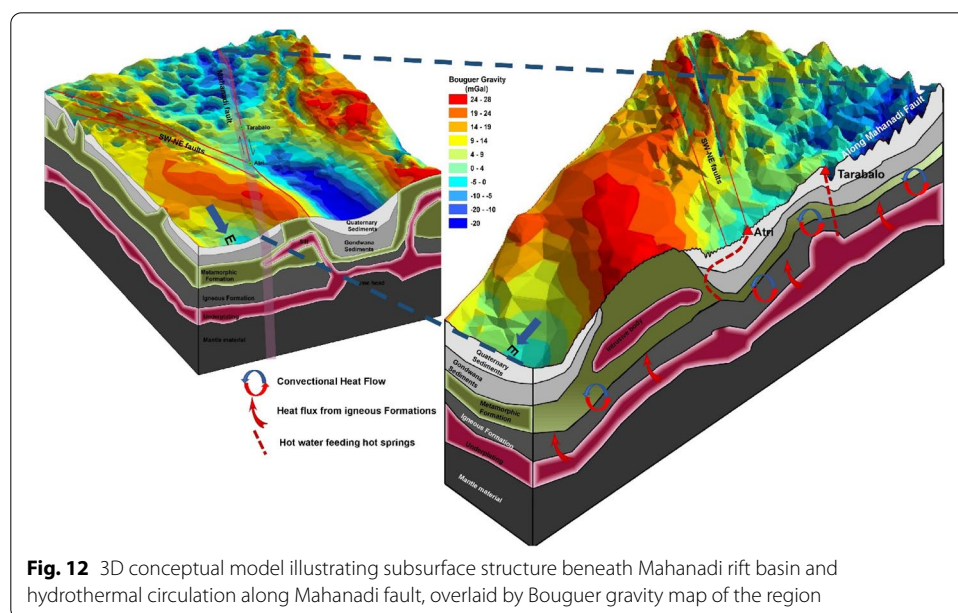

Fig. 12 3D conceptual model illustrating subsurface structure beneath Mahanadi rift basin and hydrothermal circulation along Mahanadi fault, overlaid by Bouguer gravity map of the region

heat to the fluids in the pore space of the rock formations. The Mahanadi fault itself act as the medium of water circulation along the rock formations while the local and shallow fractures connecting the Mahanadi fault feed the hot springs of the study area.

Globally, some high heat flow regions along intracontinental rifts are identified as potential geothermal reservoirs, like Fang hot springs of northern Thailand (Wood et al. 2018) and Rhine rift basin (Bachler et al. 2003) and Dholera hot springs of Cambay basin (Sircar et al. 2015). Having situated in similar rifted setup, hot springs zones along the Mahanadi fault of Mahanadi rift basin can also be a potential geothermal reservoir. This can be analysed based on detailed subsurface understanding. Thus, the present gravity–magnetic study provides important information in understanding the subsurface configuration thereby the geothermal system of the region, like existence of high-density igneous intrusion, deep-seated major faults and shallow fractures that conducts hot water to surface. This detailed subsurface analysis using gravity models and schematic representations in the present study can play an important role in further development of such geothermal areas.

Conclusions

The least availability of outcrops and different phases of sedimentation in the study area act as a significant challenge to understand the subsurface geology as well as geothermal system of the region. Present integrated gravity and magnetic study has delineated the subsurface structures and their association with the geothermal system of the region. The dissection of gravity maps clearly infers that the hot springs lies on the southern flank of Mahanadi rift basin and the predominance of high-grade metamorphic and sediment formations with faulted subsurface was observed in the vicinity. The 2D and 3D gravity models delineated the presence of high-density igneous formations beneath the metamorphic and sediment formations. The huge variation in the rock formations and faulted subsurface concludes that the region has undergone multiple phases of metamorphism and sedimentation processes. The study proposes that the hot springs in a region with a series of tectonic events and altered subsurface cannot have very shallow surface geothermal reservoir with radiogenic heat source as the sole contributor of heat to the geothermal system. The similarity in chemical composition of the hot waters, existence of both the hot springs (Atri and Tarabalo) along the Mahanadi fault and subsurface density models reveal that both the hot springs are interlinked by the deep-seated regional fault. Thus, the present study inferred some of the critical aspects related to the evolution and subsurface configuration of the hot springs along the southern flank of the Mahanadi graben, such as: (1) high heat flow at the hot springs region is the cumulative effect of the radiogenic heat of the metamorphosed rock and that of the deeper igneous intrusion while the later can be termed as primary heat source with the former having minuscule contribution; (2) the igneous intrusion are inferred to be sill type feature due to underplating formed during India–Antarctica rifting; (3) the pore spaces in the rock act as storage unit while the deep-seated regional fault acts as the primary pathway for the flow of hot fluid between the hot springs; (4) some of the local and shallow faults or fissures in the hot springs region are connected to this main deep-seated regional fault to transport the hot fluid, however, other shallow fractures in the surrounding regions are not linked to the deeper regional fault.

Abbreviations

2D: Two dimensional; 3D: Three dimensional; EGMB: Eastern Ghats Mobile Belt; GRS67: Geodetic Reference System 1967; IGRF: International Geomagnetic Reference Field; TMF: Total magnetic field; RTP: Reduce-to-pole; RTE: Reduce-to-equator; FFT: Fast Fourier transform; SI: Structural index.

Authors' contributions

AKB: design of the study, data acquisition, analysis, interpretation, modelling and original draft preparation; AM: conception and design of the study, formulation of research goals, arranging research fund, interpretation, supervision, and revising the manuscript. Both authors read and approved the final manuscript.

Availability of data and materials

Data supporting the findings are available from the authors upon request.

Declarations

Competing interests

We (the authors) declare that there are no competing interests associated with the research.

References

Artemieva IM, Thybo H, Jakonsen K, Sorensen NK, Nielsen LSK. Heat production in granitic rocks: global analysis based on new data compilation GRANITE2017. Earth-Sci Rev. 2017;172:1–26.

Bachler D, Kohl T, Rybach L. Impact of graben-parallel faults on hydrothermal convection—Rhine Graben case study. Phys Chem Earth. 2003;28:431–41.

Baksi AK. Petrogenesis and timing of volcanism in the Rajmahal flood basalt province, northeastern India. Chem Geol. 1995;121:73–90.

Baranov V. A new method for interpretation of aeromagnetic maps; pseudo-gravimetric anomalies. Geophysics. 1957;22:359–82.

Baranwal VC, Sharma SP. Integrated geophysical studies in East-Indian Geothermal Province. Pure Appl Geophys. 2006;163:29–227.

Behera L, Sain K, Reddy PR. Evidence of underplating from seismic and gravity studies in the Mahanadi delta eastern India and its tectonic significance. J Geophys Res Solid Earth. 2004;109:1–25.

Bhattacharya S, Chaudhary AK, Teixeira W. Mafic dykes at the southwestern margin of Eastern Ghats belt: evidence of rifting and collision. J Earth Syst Sci. 2010;119:815–23.

Bhattacharyya PK. Continous spectrum of the total magnetic field anomaly due to prismatic body. Geophysics. 1966;XXXI(1):97–121.

Bose S, Gupta S. Strain partitioning along the Mahanadi shear zone: implications for paleo-tectonics of the Eastern Ghats Province, India. J Asian Earth Sci. 2018;157:268–82.

Bose S, Das A, Samantaray S, Banerjee S, Gupta S. Late tectonic reorientation of lineaments and fabrics in the northern Eastern Ghats Province, India: evaluating the role of the Mahanadi Shear Zone. J Asian Earth Sci. 2020;201:104071.

Central Ground Water Board, Govt. of India. Ground water information booklet of Khurdha district. Orissa: Ministry of Water Resources; 2013a.

Central Ground Water Board, Govt. of India. Ground water information booklet of Nayagarh District. Orissa: Ministry of Water Resources; 2013b.

Chandrasekharam D, Chandrshekar V. Geochemistry of thermal springs of Orissa, India. GRC Transact. 2010;34:665–7.

Chaudhuri B. Geological and mineral map of Orissa. Kolkata: Geological Survey of India; 2010.

Chetty TRK. The Eastern Ghats Mobile Belt, India: a collage of Juxtaposed Terranes. Gondwana Res. 2001;4:319–28.

Cloetingh S, Burov E, Matenco L, Beekman F, Roure F, Ziegler PA. The moho in extensional tectonic settings: insights from thermo-mechanical models. Tectonophysics. 2013;609:558–604.

Dasgupta S, Bose S, Das K. Tectonic evolution of the Eastern Ghats Belt, India. Precambrian Res. 2013;227:247–58.

Elizondo ED, Atekwana EA, Atekwana EA, Tsokonombwe G, Davila DAL. Medium to low enthalpy geothermal reseroirs estimated from geothermometry and mixing models of hot springs along the Malawi Rift Zone. Geothermics. 2021;89:101963.

Fedorov LV, Grikurov GE, Kurinin RG, Masolov VN. Crustal structure of the Lambert Glacier area from geophysical data. In: Craddock C, editor. Antarctic geoscience, vol. 93. Madison: University of Wisconsin Press; 1982. p. 1–936.

Frehner M, Schmalholz SM. Numerical simulations of parasitic folding in multilayers. J Struct Geol. 2006;28(9):97–106.

Friedmann SJ, Burbank DW. Rift basins and supradetachment basins: intracontinental extensional end-members. Basin Res. 1995;7:109–27.

Gogte BS, Ramana YV. Physical and elastic properties of some khondalites from the Estern Ghat Belt of Peninsular India. Can J Earth Sci. 1976;13(9):1333–42.

Guo L, Meng X, Chen Z, Li S, Zheng Y. Preferential filtering for gravity anomaly separation. Comput Geosci. 2013;51:247–54.

Gupta H, Roy S. Geothermal energy: an alternate resource for the 21st century. Amsterdam: Elsevier; 2007. p. 52–4.

Hasterok D, Webb J. Research paper on the radiogenic heat production of igneous rocks. Geosci Front. 2017;8:919–40.

Hochstein MP. Crustal heat traMorgannsfer in the Taupo Volcaniz Zone (New Zealand): comparison with other volcanic arcs and explanatory heat source models. J Volcanol Geoth Res. 1995;68:117–51.

Hofmann J. Fragmente intragondwanischer Rifte als Werkzeug der Gondwana-Rekonstruktion—das Beispeil des Lambert-Mahanadi-Riftes (Ostantarktika-Peninsular Indien). Neues Jahrb Geol Palaeontol Abh. 1996;199:33–48.

Jain S. Total magnetic field reduction—the pole or equator? A model study. Can J Explor Geophys. 1988;24(2):185–92.

Koptev A, Calais E, Burov E, Leroy S, Gerya T. Dual continental rift system generated by plume-lithosphere interaction. Nature Geoscienes. 2015;8:388–92.

Kumar PS, Menon R, Reddy GK. The role of radiogenic heat production in the thermaal evolution of a Proterozoic granulite-facies orogenic belt: eastern Ghats, Indian Shield. Earth Planet Sci Lett. 2007;254:39–54.

Laske G, Masters G, Ma Z, Pasyanos ME. Update on CRUST1.0—A 1-degree global model of Earth's crust. Geophy Res Abstr. 2012;15:2013–658.

Lisker F. The evolution of the geothermal gradient from Lambert Graben and Mahanadi Basin—a contribution to the Indo-Antarctic rift debate. Gondwana Res. 2004;7:363–73.

Lisker F, Fachmann S. Phanerozoic history of the Mahanadi region, India. J Geophys Res Solid Earth. 2001;106(B10):22027–50. https://doi.org/10.1029/2001jb000295.

Lysak SV. Terrestrial heat flow of continental rifts. Tectonophysics. 1987;143:31–41.

Lysak SV. Heat flow variation in continental rifts. Tectonophysics. 1992;208:309–23.

Mahalik N. Lithology and tectonothermal history of the Precambrian rocks of Orissa along the eastern coast of India. J SE Asian Earth Sci. 1996;14:209–19.

Maitra A, Singh A, Keesari T, Sharma SP, Gupta S. Elevated equilibrium geotherm in stable continental shield: evidence from integrated structural, hydrological, and electromagnetic studies on nonvolcanic hot springs in the Eastern Ghats Belt, India. J Geophys Res Solid Earth. 2020. https://doi.org/10.1029/2019JB017747.

Mandal A, Mohanty WK, Sharma SP. 3D Compact inversion of gravity data for chromite exploration—a case study from Tangarparha, Odisha, India, vol. 32. Houston: SEG International Exposition and 84th Annual Meeting; 2013. p. 2109–13.

Mandal A, Basantaray AK, Chandroth A, Mishra U. Integrated geophysical investigation to map shallow surface alteration/fracture zones of Atri and Tarabalo hot springs, Odisha, India. Geothermics. 2019;77:24–33.

Mandal A, Athul C, Basantaray AK, Mishra U. Delineation of shallow structures in Madwara igneous complex, Bundelkhand Craton, India, using gravity-magnetic data: Implication of tectonic evolution and mineralization. J Earth Syst Sci. 2020;129:90.

McCarthy KT, Pichler T, Price RE. Geochemistry of Champgne Hot Springs shallow hydrothermal vent field and associated sediments, Dominica, Lesser Antillles. Chem Geol. 2005;224:55–68.

McKenzie D. Some remarks on the development of sedimentary basins. Earth Planet Sci Lett. 1978;40:25–32.

Mishra DC, Chandra Sekhar D, Venkata Raju DC, Vijaya Kumar V. Crustal structure based on gravity-magnetic modelling constrained from seismic studies under Lambert Rift, Antarctica and Godavari and Mahanadi rifts, India and their interrelationship. Earth Planet Sci Lett. 1999;172:287–300.

Morgan P. Constraints on rift thermal processes from heat flow and uplift. Tectonophysics. 1983;94:277–98.

Njinju EA, Kolawole F, Atekwana EA, Stamps DS, Atekwana EA, Abdelsalam MG, Mickus KL. Terrestrial heat flow in the Malawi Rift Zone, East Aftric: implications for tectono-thermal inheritance in continental rift basin. J Volcanol Geotherm Res. 2019;387:106656.

Qureshy MN, Rao SDV, Bhatia SC, Aravamadhu PS, Subrahmanyam C. Gravity bases established in India by N.G.R.I. Part IV. Geophys Res Bull. 1973;2:136–52.

Ramberg H. Evolution of drag folds. Geol Mag. 1963;100(2):97–106.

Rao GV, Rao RUM. Heat flow in Indian Gondwana basins and heat production of their basement rocks. Tectonophysics. 1983;91:105–17.

Reid AB, Allsop JM, Granser H, Millet AJ, Somerton IW. Magnetic interpretation in three dimensions using Euler deconvolution. Geophysics. 1990;55:80–91.

Roest WR, Pilkington M. Identifying remanent magnetization effects in magnetic data. Geophysics. 1993;58:653–9.

Sarkar RK, Saha DK. A note on the lithosphere thickness and heat flow density of the Indian Craton from MAGSAT data. Acta Geophys. 2006;54:198–204.

Sharma RS. Lecture note in Earth Sciences: Cratons and fold belts of India. Berlin: Springer; 2009.

Sircar A, Shah M, Sahajpal S, Vaidya D, Dhale S, Chaudhary A. Geothermal exploration in Gujarat: case study from Dholera. Geotherm Energy. 2015;3:22.

Smith WHF, Sandwell DT. Global seafloor topography from satellite altimetry and ship depth soundings. Science. 1997;277:1957–62.

Spector A, Grant FS. Statistical models for interpreting aeromagnetic data. Geophysics. 1970;35(2):293–302.

Spiess FN, Macdonald KC, Atwater T, Ballard R, Crranza A, Cordoba D, Cox C, Garcia VMD, Francheteau J, Guerreo J, Hawkins J, Haymon R, Hessler R, Juteau T, Kastner M, Larson R, Luyendyk B, Macdougall JD, Miller S, Normark W, Orcutt J, Rangin C. East Pacific Rise: hot springs and geophysical experiments. Science. 1980;207:4438.

Srivastava R, Basantaray AK, Mandal A. Improved compact inversion approach for 2D gravity data modelling using probabilistic bounds. Eur Assoc Geosci Eng. 2018. https://doi.org/10.3997/2214-4609.201801464.

Talwani M, Worzel JL, Landisman M. Rapid gravity computaions for two-dimensional bodies with application to the Mendocino submarine fracture zone. J Geophys Res. 1959;64:1.

Thompson DT. EULDPH: a new technique for making depth estimates from magnetic data. Geophysics. 1982;47:31–7.

Veevers JJ, Tewari RC. Gondwana master basin of Peninsular India between Tethys and the interior of the Gondwanal- and province of Pangea. Mem Geol Soc Am. 1995;187:1–73. https://doi.org/10.1130/0-8137-1187-8.1.

Won IJ, Bevis M. Computing gravitational and magnetic anomalies due to polygon: algorithms and Fortran subrou- tines. Geophysics. 1987;52(2):232–8.

Wood SH, Kaewsomwang P, Singharajwarapan S. Geologic framework of the Fang Hot springs area with emphasis on structure, hydrology and geothermal development, Chiang Mai Province, northern Thailand. Geotherm Energy. 2018;6:3. https://doi.org/10.1186/s40517-017-0087-7.

Yadav K, Sircar A. Geothermal energy provinces in India: a renewable heritage. Int J Geoheritage Parks. 2020. https://doi.org/10.1016/j.ijgeop.202012.002.

Yadav K, Sircar A. Modelling of earth's geothermal subtle traps using gravity Euler deconvolution. Model Earth Syst Environ. 2021;7:2769–77.

Zimik HV, Farooq SH, Prusty P. Geochemical evaluation of thermal springs in Odisha, India. Environ Earth Sci. 2017;76:593.

Publisher's Note